

Cross-correlation between *Planck* CMB lensing potential and galaxy catalogues from HELP

Chandra Shekhar Saraf,¹★ P. Bielewicz,² M. Chodorowski¹

¹*Nicolaus Copernicus Astronomical Centre, Polish Academy of Sciences, ul. Bartycka 18, Warsaw 00-716, Poland*

²*National Centre for Nuclear Research, ul. L. Pasteura 7, Warsaw 02-093, Poland*

Accepted XXX. Received YYY; in original form ZZZ

ABSTRACT

We present the study of cross-correlation between Cosmic Microwave Background (CMB) gravitational lensing potential map released by the *Planck* collaboration and photometric redshift galaxy catalogues from the *Herschel* Extragalactic Legacy Project (HELP), divided into four sky patches: NGP, *Herschel* Stripe-82, and two halves of SGP field, covering in total $\sim 660 \text{ deg}^2$ of the sky. We estimate the galaxy linear bias parameter, b_0 , from joint analysis of cross-power spectrum and galaxy auto-power spectrum using Maximum Likelihood Estimation technique to obtain values ranging from 0.70 ± 0.01 for SGP Part-2 to 1.02 ± 0.02 for SGP Part-1 field. We also estimate the amplitude of cross-correlation and find the values spanning from 0.67 ± 0.18 for SGP Part-2 to 0.80 ± 0.23 for SGP Part-1 field, respectively. For NGP and SGP Part-1 fields the amplitude is consistent with the expected value for the standard cosmological model within $\sim 1 \sigma$, while for *Herschel* Stripe-82 and SGP Part-2 we find the amplitude to be smaller than expected with $\sim 2 \sigma$ deviation. We perform several tests on various systematic errors to study the reason for the deviation, however, value of the amplitude turns out to be robust with respect to these errors. The only significant change in the amplitude is observed when we replace the minimum-variance CMB lensing map, used in the baseline analysis, by the lensing map derived from the CMB temperature map with deprojected thermal Sunyaev-Zeldovich signal.

Key words: gravitational lensing: weak – methods: data analysis – cosmology: cosmic background radiation – cosmology: observations

1 INTRODUCTION

The Cosmic Microwave Background (CMB) has given us valuable insights into our Universe and the parameters that govern it and its evolution. We have entered an era of precision cosmology over the last two decades and one of the key contributors to this was the precise measurements of the CMB (Planck Collaboration et al. 2020a; Planck Collaboration et al. 2020b; Planck Collaboration et al. 2020c). This has helped to establish the standard model of cosmology and theory of large-scale structure (LSS) formation. Inhomogeneities generated during the period of inflation developed into the structures we see today through gravitational collapse. Therefore, by studying the anisotropies in the CMB and large-scale structure, we are able to infer the characteristics of the Universe at primordial times.

CMB photons traveling from the surface of the last scattering to us get deflected by matter inhomogeneities - an effect known as gravitational lensing. This effect changes the observed statistical properties of the CMB and alters the picture of the early Universe.

On the other hand, these distortions carry also information about the LSS. The gravitational lensing causes deflections of CMB photons, with a typical amplitude of $2'$ (Lewis & Challinor 2006). These statistical signatures of the lensed CMB field can be exploited to reconstruct the lensing potential of the matter overdensities (Zaldarriaga & Seljak 1999; Hu 2001; Hu & Okamoto 2002) and learn about the large-scale structure of the Universe (Lewis & Challinor 2006).

The map of the projected lensing potential can be reconstructed from CMB temperature and polarisation data (Millea et al. 2021; Darwish et al. 2021a; Planck Collaboration et al. 2020c; Omori et al. 2017). Since the CMB lensing is an integrated quantity along the line of sight, it does not provide direct information on the evolution of the large-scale gravitational potential. However, this information can be obtained from cross-correlation between the lensing map of CMB and tracers of LSS with known redshift. Since galaxies reside in dark matter halos (Mo et al. 2010) they are good tracers of structures causing gravitational lensing of CMB. Cross-correlation studies can be used to determine the amplitude of structure at different redshifts (Peacock & Bilicki 2018; Doux et al. 2018), measure galaxy groups and cluster masses (Gupta

★ E-mail: cssaraf@camk.edu.pl (CSS)

& Reichardt 2021; Raghunathan et al. 2019; Planck Collaboration et al. 2016) and study the relation of luminous and dark matter (Han et al. 2019; Raghunathan et al. 2018).

Many cross-correlation studies have been performed over the past with optical catalogues like Sloan Digital Sky Survey (SDSS) (Singh et al. 2020), Dark Energy Survey (DES) (Omori et al. 2019b; Omori et al. 2019a), Wide-Field Infrared Survey Explorer (WISE) (Krolewski et al. 2021; Krolewski et al. 2020; Goto et al. 2012), Two Micron All Sky Survey (2MASS) (Bianchini & Reichardt 2018) and Subaru Hyper Suprime-Cam (Marques et al. 2020; Namikawa et al. 2019) and with radio catalogues from Low-Frequency Array (LOFAR) (Alonso et al. 2021). Most of the wide-area galaxy surveys in visible/near-infrared or radio wavebands have objects with redshift slightly greater than one. Thus, only a fraction of the CMB lensing signal can be picked up through cross-correlations. Many such studies have been reported by a number of authors involving CMB lensing and galaxy density maps (Darwish et al. 2021b; Cao et al. 2020; Aguilar Faúndez et al. 2019; Giusarma et al. 2018; Schmittfull & Seljak 2018; Pullen et al. 2015; Cawthon et al. 2015; Kuntz 2015). Cross-correlation studies have also been reported between CMB lensing and quasar density maps (Zhang et al. 2021; DiPompeo et al. 2015; Han et al. 2019) as well as high-redshift sub-millimeter sources from the *Herschel* Astrophysical Terahertz Large Area Survey (H-ATLAS) have also been used to perform such studies (Bianchini et al. 2015 and Bianchini et al. 2016).

In this paper, we present the first study of cross-correlation between *Planck* CMB lensing potential (Planck Collaboration et al. 2020c) and galaxy catalogues from *Herschel* Extragalactic Legacy Project (HELP; Shirley et al. 2019, 2021). HELP catalogue is a combination of many surveys, mostly in visible and near-infrared bands, which also includes galaxies observed in *Herschel* fields. As such it does not overlap with the H-ATLAS catalogue consisting mostly of far-infrared objects. The number of objects from the HELP catalogue in our study is orders of magnitude larger compared to the catalogue used by Bianchini et al. (2015) and Bianchini et al. (2016).

We present the theoretical background in section 2 and describe the *Planck* lensing data and HELP data used in our study in section 3. In section 4, there are presented the procedure for estimation of power spectra and errors, as well as described our numerical setup employed for validation of the procedure. The method used for the estimation of parameters is described in section 5. Finally we present our results in section 7 with further discussions in section 8. At last, we summarise our results in section 9.

In this paper, we adopt the flat Λ CDM cosmology with best-fit *Planck* + WP + highL + lensing cosmological parameters, as described in Planck Collaboration et al. (2020b). Here, WP refers to *WMAP* polarisation data at low multipoles, highL is the high resolution CMB data from Atacama Cosmology Telescope (ACT) and South Pole Telescope (SPT) and lensing refers to the inclusion of *Planck* CMB lensing data in the parameter likelihood.

2 THEORY

Gravitational lensing of CMB photons can be expressed as a remapping of the unlensed temperature anisotropies $\Theta(\hat{\mathbf{n}})$ in the direction $\hat{\mathbf{n}}$ (Lewis & Challinor 2006):

$$\begin{aligned}\tilde{\Theta}(\hat{\mathbf{n}}) &= \Theta(\hat{\mathbf{n}} + \nabla\phi(\hat{\mathbf{n}})) \\ &= \Theta(\hat{\mathbf{n}}) + \nabla^a\phi(\hat{\mathbf{n}})\nabla_a\Theta(\hat{\mathbf{n}}) + \mathcal{O}(\phi^2)\end{aligned}\quad (1)$$

where $\tilde{\Theta}(\hat{\mathbf{n}})$ is the lensed temperature anisotropies and $\phi(\hat{\mathbf{n}})$ is the CMB lensing potential defined as:

$$\phi(\hat{\mathbf{n}}) = -2 \int_0^{\chi_*} d\chi \frac{\chi_* - \chi}{\chi_* \chi} \Psi(\chi\hat{\mathbf{n}}, z(\chi)) \quad (2)$$

In above equation, χ_* is comoving distance to the surface of last scattering at redshift $z \simeq 1100$ and $\Psi(\chi\hat{\mathbf{n}}, z(\chi))$ is the three dimensional gravitational potential at position $\chi\hat{\mathbf{n}}$ in photon's path. The deflection angle is then given by the two dimensional gradient on the sphere, $\nabla_{\hat{\mathbf{n}}}\phi$.

The effects of gravitational lensing due to foreground matter introduces small coherent distortions in the light coming from background sources. We define dimensionless lensing convergence κ through relation to the two-dimensional Laplacian of the lensing potential:

$$\kappa(\hat{\mathbf{n}}) = -\frac{1}{2}\nabla^2\phi(\hat{\mathbf{n}}) \quad (3)$$

The lensing convergence in a given direction of the sky can be related to the line-of-sight average of the matter over-density δ (Bartelmann & Schneider 2001):

$$\kappa(\hat{\mathbf{n}}) = \int_0^{\chi_*} d\chi \frac{H(\chi)}{c} W^\kappa \delta(\chi\hat{\mathbf{n}}) \quad (4)$$

where W^κ is the lensing kernel given by

$$W^\kappa(\chi) = \frac{3\Omega_m}{2c^2} H_0^2 (1+z) \chi \frac{\chi_* - \chi}{\chi_*} \quad (5)$$

where c is the speed of light, Ω_m and H_0 are the present-day values of the matter density parameter and Hubble constant, respectively.

Similarly, the galaxy over-density $g(\hat{\mathbf{n}})$ can also be expressed as a line of sight integral of the matter over-density:

$$g(\hat{\mathbf{n}}) = \int_0^{\chi_*} d\chi \frac{H(\chi)}{c} W^g \delta(\chi\hat{\mathbf{n}}) \quad (6)$$

with W^g given as

$$\begin{aligned}W^g(\chi) &= b \frac{H(\chi)}{c} \frac{dN}{dz(\chi)} + \frac{3\Omega_m}{2c^2} H_0^2 (1+z) \chi \\ &\quad \times \int_\chi^{\chi_*} d\chi' \frac{H(\chi')}{c} \left(1 - \frac{\chi}{\chi'}\right) (\alpha(\chi') - 1) \frac{dN}{dz(\chi')}\end{aligned}\quad (7)$$

where $\frac{dN}{dz}$ stands for the redshift distribution of galaxies, b is the galaxy linear bias that relates the luminous tracers of large scale structure with the underlying matter distribution and the second term accounts for the gravitational magnification of background objects by foreground sources (magnification bias; Turner 1980). This effect depends on the slope, $\alpha(z)$, of the integral counts of sources above the flux threshold S , i.e. $N(> S) \propto S^{-\alpha}$. We estimate α as the slope of the straight line fit to $\log N(> S)$ distribution. Because the slope estimated for objects selected from the HELP catalogue used in this work is $\alpha = 1$, the magnification bias term is null. However, in Section 8 we investigate the sensitivity of the results to different values of the slope.

As we can see from Fig. 1, the lensing kernel is broad, slowly varying from $z \sim 1$ and the redshift distributions of HELP catalogue galaxies peak at $z \sim 0.4$ for NGP, at $z \sim 0.5$ for HS-82 and SGP Part-1, and at $z \sim 0.6$ for SGP Part-2; the overlap between galaxy distribution peaks and lensing kernel ensures a high correlation between the galaxy over-density and CMB lensing convergence fields.

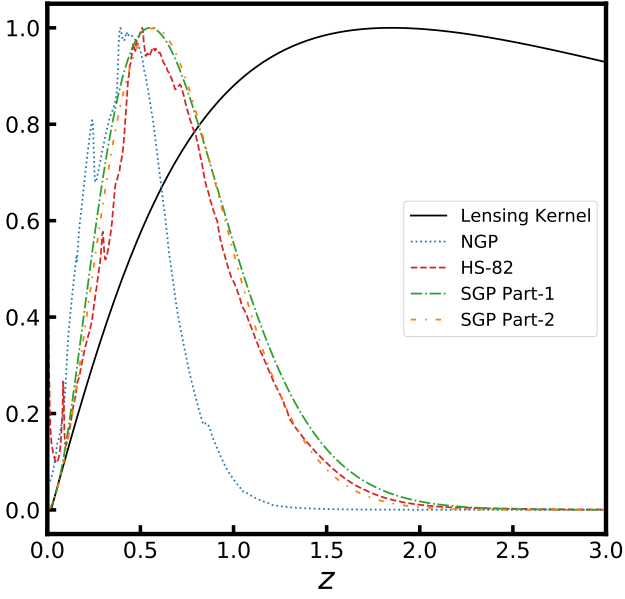


Figure 1. CMB lensing kernel W^κ compared with redshift distributions for all galaxy patches. Both lensing kernel and redshift distributions are normalised to the unit maximum.

The galaxy linear bias is, in general, a function of redshift z and halo mass, M . Since the redshift distributions are broad, we assume a galaxy linear bias dependent on redshift via $b(z) = b_0/D(z)$, where $D(z)$ is the growth factor and b_0 is galaxy linear bias parameter.

The theoretical angular power spectrum is computed under the Limber approximation (Limber 1953) as

$$C_\ell^{xy} = \int_0^{z_*} d\chi \frac{W^x(\chi)W^y(\chi)}{\chi^2} P(k = \frac{\ell+1/2}{\chi}, z(\chi)) \quad (8)$$

where $\{x, y\} = \{\kappa, g\}$, $\kappa \equiv$ convergence and $g \equiv$ galaxy over-density and $P(k = \frac{\ell+1/2}{\chi}, z(\chi))$ is the matter power spectrum generated using CAMB¹ (Lewis et al. 2000). The mean redshift probed by the cross-correlation of CMB lensing convergence and the galaxy sample is given as:

$$\langle z \rangle = \frac{\int_0^{z_*} d\chi z \frac{W^\kappa(\chi)W^g(\chi)}{\chi^2} P(k = \frac{\ell+1/2}{\chi}, z(\chi))}{\int_0^{z_*} d\chi \frac{W^\kappa(\chi)W^g(\chi)}{\chi^2} P(k = \frac{\ell+1/2}{\chi}, z(\chi))} \quad (9)$$

For our catalogue, the effective mean redshifts probed by the cross-correlation measurements are $\langle z \rangle = 0.60, 0.77, 0.76$ and 0.73 for NGP, HS-82, SGP Part-1 and SGP Part-2, respectively.

3 DATA

3.1 CMB Lensing Data

The *Planck* lensing data we use come from 2018 *Planck* data release² described in Planck Collaboration et al. (2020c). It uses the SMICA DX12 CMB maps to reconstruct the lensing potential, covering $\sim 67\%$ of the sky. For our baseline analysis, we use the

lensing convergence map derived from a minimum-variance estimate of temperature and polarization data. We also use the CMB lensing potential map derived from the thermal Sunyaev-Zeldovich deprojected SMICA map for comparison of estimated parameters. Nevertheless, because of potentially smaller contamination by Cosmic Infrared Background (CIB) emission of the minimum-variance lensing map, compared to the lensing map derived from the Sunyaev-Zeldovich deprojected map (see discussion in section 8.1), we consider the former in our baseline analysis. For the rest of the paper, we dub the minimum-variance lensing convergence map as MV and Sunyaev-Zeldovich deprojected lensing convergence map as SZ-deproj. The lensing convergence which is proportional to the two dimensional Laplacian of the lensing potential (Eq. 3), can be expressed in spherical harmonic space using the relation (Hu 2000)

$$\kappa_{\ell m} = -\frac{\ell(\ell+1)}{2} \phi_{\ell m} \quad (10)$$

The spherical harmonic coefficients for lensing convergence are provided by *Planck* data package in HEALPix³ (Górski et al. 2005) format with $N_{side} = 4096$. As small angular scales are noise-dominated we transform these coefficients to a HEALPix map with lower resolution having $N_{side} = 512$, which we use for further analysis in this study. The data package also provides noise power spectra $N_\ell^{\kappa\kappa}$ for both MV and SZ-deproj maps, along with a binary map masking parts of the sky not used in the analysis.

3.2 Galaxy Data

The *Herschel* Extra-galactic Legacy Project (HELP⁴) is a catalogue combining data from 23 extra-galactic survey fields, observed between $0.36\text{--}4.5 \mu\text{m}$. The catalogue covers $\sim 1300 \text{ deg}^2$ and contains objects with cross-matching between 51 public surveys (Shirley et al. 2019, 2021). It is worth pointing out that in our analysis we use only data from these public surveys covering *Herschel* fields, but not far-infrared data from the *Herschel* satellite itself as was done previously in similar studies (Bianchini et al. 2015, 2016). Most of the extra-galactic fields available with HELP have a very small physical surface area, making them unsuitable for our cross-correlation study. Also, because different surveys have different depths, some fields are inhomogeneous and cannot be used for our analysis. Combining these constraints we are left with three useful patches for our analysis: North Galactic Pole, South Galactic Pole, and *Herschel*-Stripe 82 (hereafter, NGP, SGP, and HS-82, respectively) covering a total of $\sim 660 \text{ deg}^2$. The details of the properties associated with each patch on the sky are provided in Table 1.

The galaxy density of the SGP field has significant variations due to the fact that the Kilo-Degree Survey (KiDS; de Jong et al. 2013) only covers approximately one-half of the SGP field. These two halves have a large difference in their mean number of objects per pixel. To avoid any effects coming from this inhomogeneity, we divide the SGP field into two parts, which we refer to as SGP Part-1 and SGP Part-2. To remove star-like sources and increase the purity of the galaxy sample, we apply two extra selection criteria, $\text{flag-gaia} \leq 2$ and $\text{stellarity} < 0.9$, which increase the likelihood that an object is a galaxy.

HELP uses the Easy and Accurate Z from Yale code (EAZY; Brammer et al. 2008) to estimate photo- z for objects. It provides

¹ <https://camb.info/>

² <https://pla.esac.esa.int/#cosmology>

³ <https://healpix.jpl.nasa.gov/>

⁴ <https://herschel.sussex.ac.uk>

Table 1. Physical properties of HELP patches. $[l, b]$ are galactic longitude and latitude respectively, N_{obj} is the number of objects in each patch, \bar{n} is the mean number of objects, f_{sky} is the fraction of sky covered by patches, and $\langle z \rangle$ is the mean redshift probed by cross-correlation computed from Eq. 9.

Patch	f_{sky}	area [deg ²]	$[l, b]$	N_{obj}	\bar{n} [gal pix ⁻¹]	\bar{n} [gal str ⁻¹]	median z	$\langle z \rangle$
NGP	0.0043	179.14	$[51^\circ, 84^\circ]$	1311549	96.908	2.426×10^7	0.45	0.60
HS-82	0.0062	255.16	$[130^\circ, -61^\circ]$	6824474	344.862	8.633×10^7	0.60	0.77
SGP Part-1	0.0020	85.83	$[12^\circ, -68^\circ]$	3151922	481.577	1.206×10^8	0.71	0.76
SGP Part-2	0.0035	145.32	$[-82^\circ, -86^\circ]$	6659404	600.975	1.504×10^8	0.71	0.73

posteriors from the photo- z pipeline for every object in the catalogue. The estimated photometric redshifts are the median values of these posteriors. We use these posteriors to build on the redshift galaxy distributions by stacking these posteriors together. The redshift distributions are shown in Fig. 1. Using these posteriors translates the errors on redshift to redshift distributions (Budavári et al. 2003). We select all objects for which the relative error on redshift, $\frac{\sigma_z}{1+z} < 0.15$ for NGP and HS-82 and $\frac{\sigma_z}{1+z} < 0.25$ for SGP Part-1 and SGP Part-2. We use a higher limit on $\frac{\sigma_z}{1+z}$ for SGP fields, because the median value of $\frac{\sigma_z}{1+z}$ for these fields is higher, i.e. 0.22, than for NGP and HS-82 fields which have the median equal to 0.15 and 0.16, respectively.

These cuts result in a final catalogue of ~ 18 million objects. Table 1 summarises the total and mean number of objects for the NGP, HS-82, and the two SGP fields. The galaxy number density of the samples used in this analysis is approximately two orders of magnitudes higher than that of the far-infrared Herschel data set used in Bianchini et al. (2015; 2016).

We build galaxy over-density maps with resolution $N_{side} = 512$ using the relation

$$g(\hat{\mathbf{n}}) = \frac{n(\hat{\mathbf{n}}) - \bar{n}}{\bar{n}} \quad (11)$$

where $n(\hat{\mathbf{n}})$ is the number of objects in a given pixel and \bar{n} is the mean number of objects per pixel. Fig. 2 shows the *Planck* lensing convergence and galaxy over-density maps for all patches, from which we have filtered out $\ell \geq 400$. It shows the part of the sky common to both galaxy fields and *Planck* convergence field. But in our analysis, we use the full lensing convergence map available (covering $\sim 67\%$), uplifting the condition of using only the common area.

4 METHODOLOGY

4.1 Power-spectra

We use the MASTER algorithm (Hivon et al. 2002) to convert from pseudo-power spectra computed from smaller fractions of the sky to the full-sky power spectra. MASTER is based on direct spherical harmonic transform to obtain an unbiased estimate of the power spectrum. The harmonic mode coupling induced by incomplete sky coverage is described by the mode coupling kernel $M_{\ell\ell}$. The ensemble average of the pseudo-power spectrum can be related to the full-sky power spectrum by

$$\tilde{C}_\ell^{xy} = \sum_{\ell'} M_{\ell\ell'} C_{\ell'}^{xy} \quad (12)$$

where C_ℓ^{xy} is the full-sky power spectrum and \tilde{C}_ℓ^{xy} is the pseudo-

power spectrum measured from data from the relation

$$\tilde{C}_\ell^{xy} = \frac{1}{2\ell+1} \sum_{m=-\ell}^{\ell} \tilde{a}_{\ell m}^x \tilde{a}_{\ell m}^{*y} \quad (13)$$

where $\tilde{a}_{\ell m}$ are the spherical harmonic coefficients from partial sky coverage and $\{x, y\} = \{\kappa, g\}$.

However, Eq. 12 cannot be inverted directly because the coupling kernel is singular for smaller fractions of sky. To avoid these singularities we bin the power spectrum in ℓ with bin-width of $\Delta\ell = 100$ and the estimator of power spectra is then given by

$$\langle \hat{C}_L^{xy} \rangle = \sum_{L'} K_{LL'}^{-1} (\langle \tilde{C}_{L'}^{xy} \rangle - \langle \tilde{N}_{L'}^{xy} \rangle) \quad (14)$$

where

$$\tilde{C}_{L'}^{xy} = \sum_{\ell'} P_{L'\ell'} \tilde{C}_{\ell'}^{xy} \quad (15)$$

and

$$K_{LL'} = \sum_{\ell'} P_{L\ell} M_{\ell\ell'} B_{\ell'}^2 Q_{\ell'L} \quad (16)$$

where L stands for the multipole bin and B_ℓ is the pixel window function that accounts for the finite size of the pixels. $P_{L\ell}$ is the binning operator expressed as:

$$P_{L\ell} = \begin{cases} \frac{1}{2\pi} \frac{\ell(\ell+1)}{\ell_{low}^{(L+1)} - \ell_{low}^{(L)}}, & \text{if } 2 \leq \ell_{low}^{(L)} \leq \ell \leq \ell_{low}^{(L+1)} \\ 0, & \text{otherwise} \end{cases} \quad (17)$$

and $Q_{\ell L}$ is the reciprocal binning operator:

$$Q_{\ell L} = \begin{cases} \frac{2\pi}{\ell(\ell+1)}, & \text{if } 2 \leq \ell_{low}^{(L)} \leq \ell \leq \ell_{low}^{(L+1)} \\ 0, & \text{otherwise} \end{cases} \quad (18)$$

In Eq. 14, \tilde{N}_L^{xy} is the pseudo noise power spectrum. In cross-correlation studies, one of the main assumption is that the noise associated with galaxy over-density and lensing convergence fields are uncorrelated. Thus, there will be no noise associated with cross-power spectrum, i.e., $N_\ell^{K\kappa} = 0$. But for auto-power spectra $C_\ell^{K\kappa}$ and $C_\ell^{g\kappa}$, we account for noise. We estimate the noise pseudo spectra from Monte Carlo simulations, with which Eq. 14 becomes

$$\hat{C}_L^{xy} = \sum_{L'} K_{LL'}^{-1} (\tilde{C}_{L'}^{xy} - \langle \tilde{N}_{L'}^{xy} \rangle_{MC}) \quad (19)$$

We estimate the full-sky power spectrum for the multipole range $0 \leq \ell \leq 1200$ using Eq. 19, while we use 7 linear bins in the multipole range $100 \leq \ell \leq 800$ in our study.

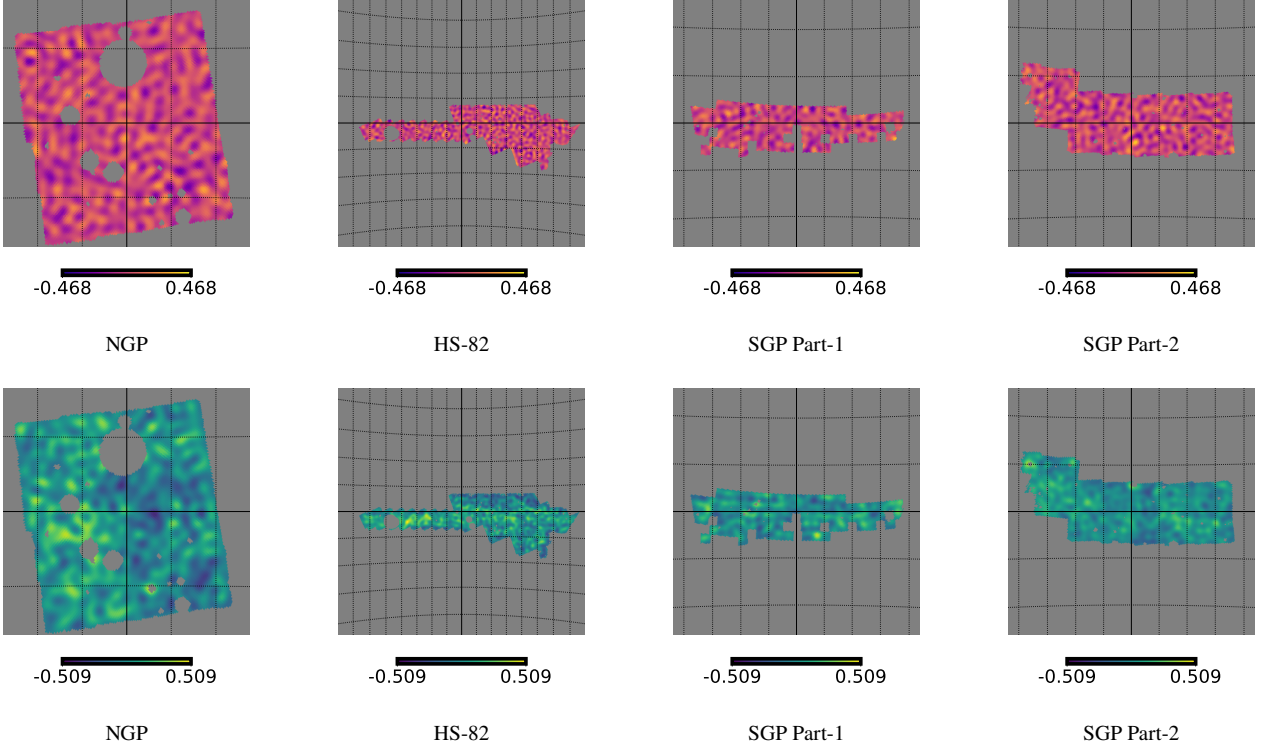


Figure 2. Convergence maps (upper row) and galaxy over-density Maps (lower row) of NGP, HS-82, SGP Part-1 and SGP Part-2 fields. Multipoles $\ell \geq 400$ have been filtered out from all maps. The grid spacing is 3° in longitude and 5° in latitude.

4.2 Errors

The errors on the power spectrum can be computed from the square root of diagonal of the analytical covariance matrix:

$$Cov_{LL'}^{AB,CD} = \frac{1}{(2\ell_{L'} + 1)\Delta\ell f_{sky}^{AB} f_{sky}^{CD}} \left[f_{sky}^{AC, BD} \sqrt{C_L^{AC} C_{L'}^{AC} C_L^{BD} C_{L'}^{BD}} + f_{sky}^{AD, BC} \sqrt{C_L^{AD} C_{L'}^{AD} C_L^{BC} C_{L'}^{BC}} \right] \delta_{LL'} \quad (20)$$

where $\{A, B, C, D\} = \{\kappa, g\}$, $\Delta\ell$ is the multipole binwidth, f_{sky}^{AB} is the fraction of sky common to fields A and B , $f_{sky}^{AC, BD}$ is the fraction of sky covered by fields AB and CD , and $\delta_{LL'}$ is the Kronecker delta. The expression of covariance matrix in Eq. 20 is not constrained by the limitation of using only the fraction of sky common to both CMB lensing convergence and galaxy surveys. The detailed derivation of the covariance matrix can be found in appendix A. We use the expression Eq. 20 for covariance in estimation of parameters from likelihood analysis discussed in section 5.

Fig. 3 shows the correlation matrices obtained from simulations of HS-82 field. All correlation matrices are dominated by diagonal elements and the off-diagonal terms are smaller in comparison. Thus the assumed diagonal approximation holds strongly for our purpose and also serves as a good way to save some computation time.

4.3 Simulations

To validate the numerical algorithms and to check that power-spectra and parameters estimated do not contain any systematic error, we

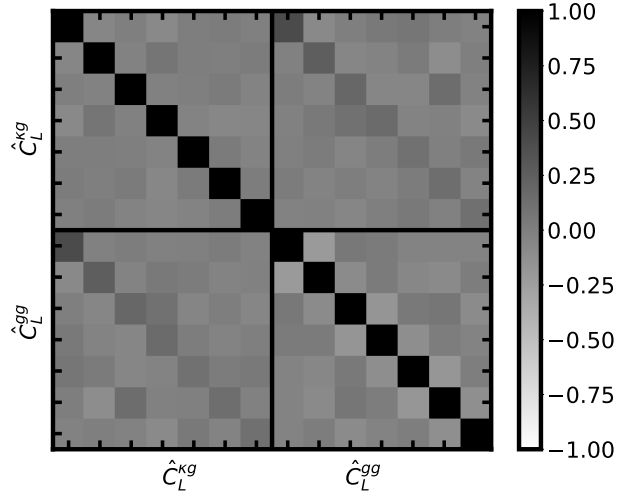


Figure 3. Correlation matrices constructed from the covariance matrix mentioned in Eq. 25 for HS-82 field. The correlation matrix is dominantly diagonal.

simulate maps of both CMB convergence and galaxy over-density fields with statistical properties consistent with observations. We introduce a known degree of correlation in theoretical power-spectra (Eq. 8), using the relation (Kamionkowski et al. 1997):

$$\begin{aligned} \kappa_{\ell m} &= \xi_1 (C_\ell^{\kappa\kappa})^{1/2}; \\ g_{\ell m} &= \xi_1 \frac{C_\ell^{\kappa g}}{(C_\ell^{\kappa\kappa})^{1/2}} + \xi_2 \left[C_\ell^{gg} - \frac{(C_\ell^{\kappa g})^2}{C_\ell^{\kappa\kappa}} \right]^{1/2} \end{aligned} \quad (21)$$

For each ℓ and $m > 0$, ξ_1 and ξ_2 are two complex random numbers drawn from a Gaussian distribution with unit variance and for $m = 0$, the random numbers are real and normally distributed.

We simulate these maps to also include noise. For convergence noise maps, we used the minimum variance noise power spectrum $N_\ell^{\kappa\kappa}$, provided in the *Planck* 2018 data package. To account for noise associated with galaxy over-density maps, we simulate galaxy number count maps where the value in each pixel is drawn from a Poisson distribution with mean

$$\lambda(\hat{\mathbf{n}}) = \bar{n}(1 + g(\hat{\mathbf{n}})) \quad (22)$$

where \bar{n} is the mean number of sources per pixel and $g(\hat{\mathbf{n}})$ is the corresponding simulated galaxy over-density map with only signal. When simulating Gaussian fields, it often leads to some pixels with values $g < -1$ from which Poisson samples cannot be drawn. In cases of simulations with some pixels being $g < -1$, we reject those simulated maps. The galaxy number count map, thus obtained, is then converted to the over-density map using Eq. 11. The statistical properties of noise simulated in this way are the same as for data.

From maps simulated with this procedure, we recover the full sky power-spectra as mentioned in section 4.1. The mean power spectrum is computed as

$$\bar{C}_L^{xy} \equiv \langle \hat{C}_L^{xy} \rangle = \frac{1}{N} \sum_{i=1}^N \hat{C}_L^{xy,i} \quad (23)$$

where $\hat{C}_L^{xy,i}$ represents the power spectrum estimate for i^{th} simulation and N is the number of simulations. The associated errors are computed from the covariance matrix as

$$\Delta \bar{C}_L^{xy} = \left(\frac{Cov_{LL}^{xy}}{N} \right)^{1/2} \quad (24)$$

where the covariance matrix is evaluated from simulations:

$$Cov_{LL'}^{xy} = \frac{1}{N-1} \sum_{i=1}^N (\hat{C}_L^{xy,i} - \bar{C}_L^{xy})(\hat{C}_{L'}^{xy,i} - \bar{C}_{L'}^{xy}) \quad (25)$$

5 LIKELIHOOD ANALYSIS AND PARAMETER ESTIMATION

We estimate two parameters in our study: galaxy linear bias parameter b_0 and amplitude of the cross-power spectrum, A . The cross-power spectrum depends on the product of galaxy linear bias parameter b_0 and amplitude A . To break this degeneracy, we use a likelihood function containing galaxy auto-power spectrum, which scales as b_0^2 as well as cross-power spectrum. This joint likelihood function is given as:

$$\begin{aligned} \mathcal{L}(\hat{C}_L | b_0, A) &= \frac{1}{\sqrt{(2\pi)^{N_L} \det(Cov_{LL'})}} \times \\ &\times \exp \left\{ -\frac{1}{2} [\hat{C}_L - C_L(b_0, A)] (Cov_{LL'})^{-1} [\hat{C}_L - C_L(b_0, A)] \right\} \end{aligned} \quad (26)$$

where N_L is the number of multipole bins. \hat{C}_L is 14-element data vector constructed from estimated galaxy auto-power spectrum \hat{C}_L^{gg} and cross-power spectrum $\hat{C}_L^{\kappa g}$ as

$$\hat{C}_L = (\hat{C}_L^{\kappa g}, \hat{C}_L^{gg}) \quad (27)$$

$C_L(b, A)$ is the joint power spectrum template, used in extracting parameters b and A , defined as

$$C_L(b_0, A) = (AC_L^{\kappa g}(b_0), C_L^{gg}(b_0)) \quad (28)$$

The covariance matrix $Cov_{LL'}$ in Eq. 26 is given as

$$Cov_{LL'} = \begin{bmatrix} Cov_{LL'}^{\kappa g, \kappa g} & Cov_{LL'}^{\kappa g, gg} \\ Cov_{LL'}^{\kappa g, gg} & Cov_{LL'}^{gg, gg} \end{bmatrix} \quad (29)$$

where the covariance $Cov_{LL'}^{\kappa g, gg}$ which accounts for the correlation between the CMB convergence and galaxy density fields, is given by Eq. 20 with $(A, B, C, D) \equiv (\kappa, g, g, g)$. Similarly, expressions for $Cov_{LL'}^{\kappa g, \kappa g}$ and $Cov_{LL'}^{gg, gg}$ is evaluated using $(A, B, C, D) \equiv (\kappa, g, \kappa, g)$ and $(A, B, C, D) \equiv (g, g, g, g)$, respectively.

The cosmological parameters, except for those to be determined, are kept constant with values from our fiducial background cosmology described in [Planck Collaboration et al. \(2020b\)](#). We use the publicly available package EMCEE ([Foreman-Mackey et al. 2013](#)) to sample the parameter space. We define the best-fit values of parameters to be the median of the posterior distribution after marginalizing over other free parameters. We additionally report the 1σ confidence intervals of the estimated best-fit values.

6 PIPELINE VALIDATION

We simulate 500 maps with the procedure outlined in section 4.3 to validate our pipeline for estimating power spectra and parameters. The upper panel of Fig. 4 shows the reconstructed power spectra averaged over 500 simulations using our algorithm. The lower panel shows the relative difference between the theoretical power spectrum used for simulations and the recovered power spectra from simulations. The power spectra are very well recovered within one standard error.

In Fig. 5 we also show the comparison of errors on cross-power spectrum estimated for simulations from the square root of the diagonal of Eq. 25 and errors estimated analytically from Eq. 20.

To check whether estimation of the parameters is unbiased in Fig. 6 we show the comparison of true values of the parameters that we use in simulations, i.e. $b_0 = 2$ and $A = 1$ (red lines), with the distribution of the parameters estimated from 500 simulations of HS-82 field with the procedure mentioned in section 5. As we can see the distribution of parameters is very well centered on the true values used for simulations which prove that our algorithm provides an unbiased estimation of the parameters. We find similar results for other fields as well.

7 RESULTS

We now present the results of extracting power spectrum and galaxy linear bias parameter b_0 and amplitude of cross-power spectrum A using the procedures described in sections 4 and section 5.

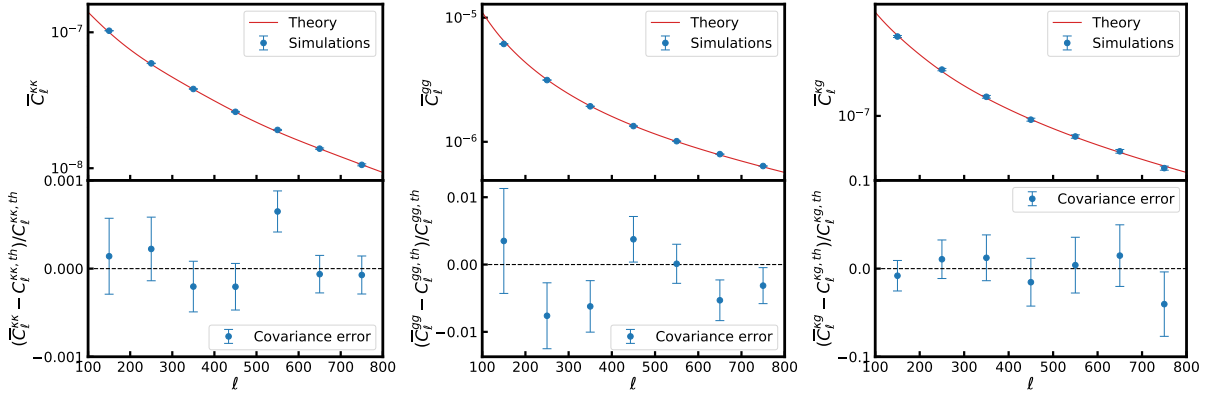


Figure 4. *Top* : Average power spectra reconstructed for 500 simulations. The red line represents the theoretical power spectrum used for simulations. *Bottom* : Error estimated for the reconstructed simulated average power spectra relative to the theoretical power spectrum. *Left to Right* : CMB lensing convergence power spectrum, galaxy auto-power spectrum, and cross-power spectrum

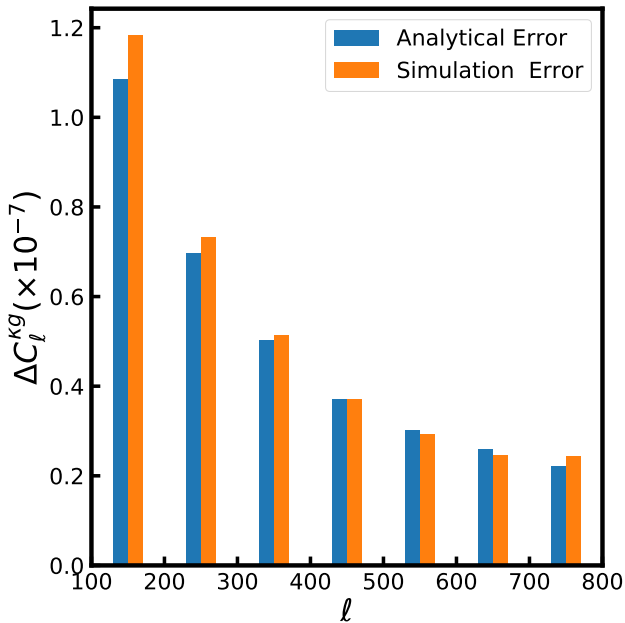


Figure 5. Comparison of simulation (orange) and analytical (blue) errors for cross-power spectrum. The orange bars are computed from the square root of the diagonal of Eq. 25. The blue bars are calculated from Eq. 20

7.1 Power Spectra

The noise subtracted galaxy auto-power spectra and cross-power spectra for all four HELP fields are shown in Fig. 7. The errors are estimated from the diagonal of the analytical covariance matrix described in section 4.2 using the best fit values of b_0 and A .

Before going over parameter estimation, we discuss the results of the null hypothesis. We calculate the probability that the estimated signal is consistent with no correlation between galaxy over-density and lensing convergence fields. The χ^2_{null} values are calculated using

$$\chi^2_{null} = \hat{C}_L^{kg} (Cov_{LL'}^{kg})^{-1} \hat{C}_L^{kg} \quad (30)$$

The χ^2_{null} values for cross-power spectra from all four patches and

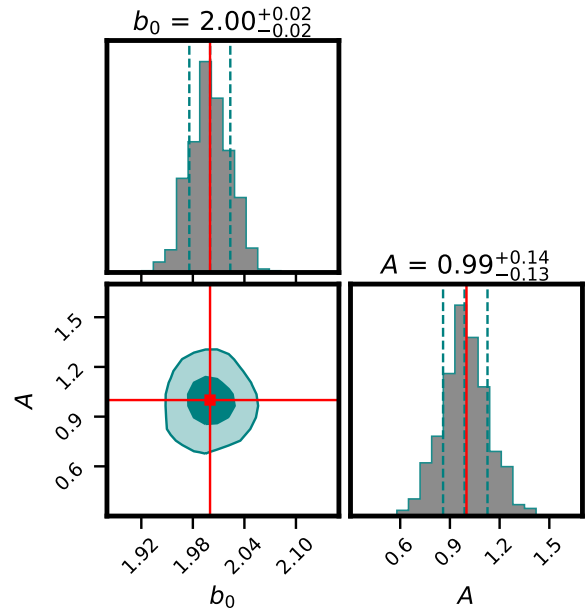


Figure 6. Distribution of estimated parameters b_0 and A for 500 simulations of HS-82 field. The lighter and darker contours represent the 68% and 95% confidence levels. The three vertical lines are the median value of marginalised posteriors and $\pm 1\sigma$ errors. The red lines show the true values of parameter $b = 2$ and $A = 1$ used for simulations.

their associated p -values are presented in Table 2 with $\nu = 7$ being the number of degrees of freedom.

Another null test we perform is cross-correlating galaxy shot noise, estimated by a jackknifing approach (Ando et al. 2018; Bianchini & Reichardt 2018) with true *Planck* CMB convergence map. We randomly split the galaxy catalogue into two over-density maps δ_g^1 and δ_g^2 . Then, the map $(\delta_g^1 + \delta_g^2)/2$ contains both signal and noise, while $(\delta_g^1 - \delta_g^2)/2$ is noise-only map. Fig. 8 shows the mean correlation of 500 galaxy shot noise obtained from jackknifing method for all patches with lensing convergence map. The error bars are computed from the covariance matrices obtained from these 500 correlations. No significant cross-correlation signal is detected for any patch and we obtain $\chi^2/\nu = 0.083, 0.537, 0.429$ and 0.283 with $\nu = 7$ degrees of freedom, with probability of no correla-

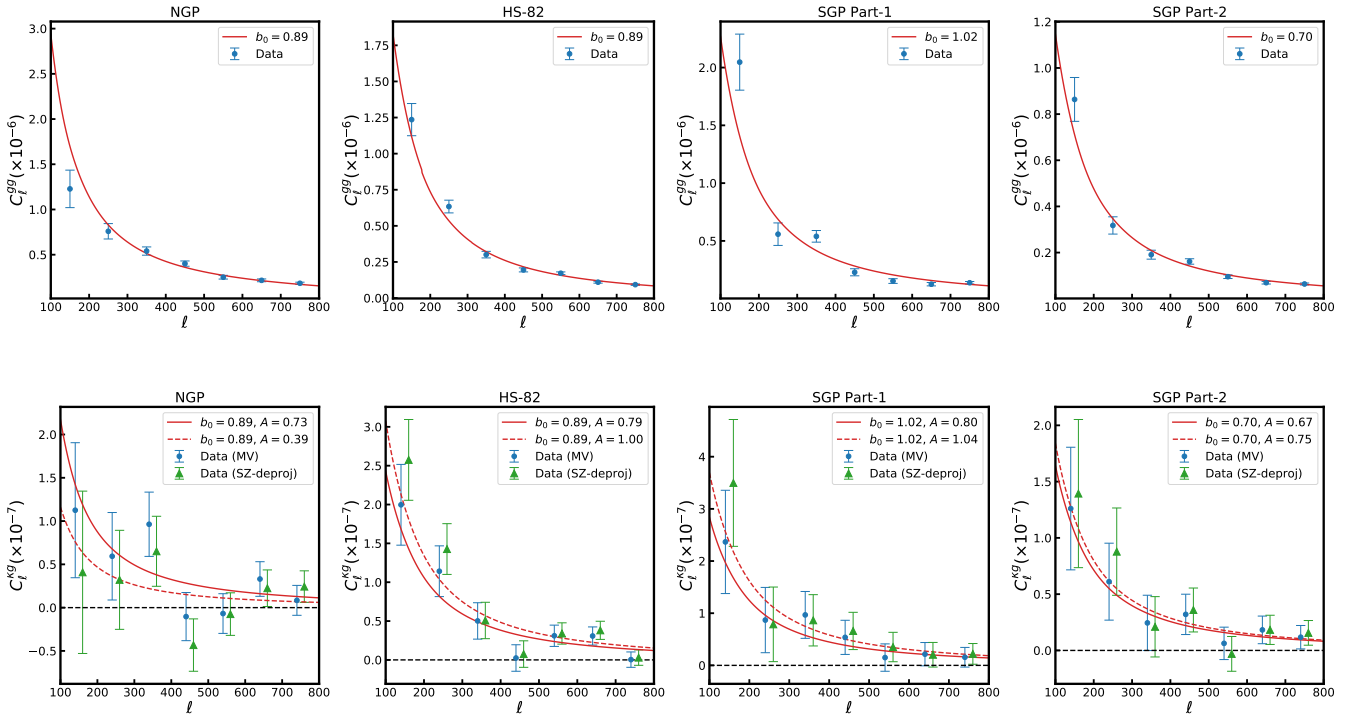


Figure 7. Galaxy auto-power spectra (*Top*) and cross-power spectra (*Bottom*) for HELP fields. The blue circles represent the measurements of cross-correlation signal using MV map while green triangles are for SZ-deproj map. The red solid line is the theoretical power spectrum computed using the best-fit values obtained from likelihood analysis using MV map and the red dashed line is the theoretical line for SZ-deproj map.

Table 2. Result of no correlation hypothesis rejection for HELP patches using MV and SZ-deproj convergence maps.

Patch	MV		SZ-deproj	
	χ^2_{null}/ν	p -value	χ^2_{null}/ν	p -value
NGP	13.4/7	6.32×10^{-2}	8.14/7	0.32
HS-82	41.5/7	6.57×10^{-7}	54.9/7	1.59×10^{-9}
SGP Part 1	16.9/7	1.80×10^{-2}	19.5/7	6.69×10^{-3}
SGP Part 2	16.4/7	2.16×10^{-2}	17.7/7	1.36×10^{-2}

tion $p = 0.99, 0.81, 0.88$ and 0.96 for NGP, HS-82, SGP Part-1 and SGP Part-2, respectively.

7.2 Galaxy linear bias parameter and Amplitude

Estimated values of parameters for real data using MV lensing map are presented in Table 3 and those using SZ-deproj lensing map are presented in Table 4. Constraints on galaxy linear bias parameter and amplitude of cross-power spectrum were obtained by sampling the likelihood function given in Eq. 26 for the joint power spectrum \hat{C}_L . We also compute these parameters by independently sampling the likelihood function for measured galaxy auto-power spectrum, \hat{C}_L^{gg} and cross-power spectrum, \hat{C}_L^{kg} only.

To give some idea on goodness of fit of theoretical power spectra to observations in the tables we provide also χ^2 and p -values. We evaluate the χ^2 values using the expression: $\chi^2 = [\hat{C}_L^{kg} - A^{bf} C_L^{kg}(b_0^{bf})](Cov_{LL}^{kg})^{-1}[\hat{C}_L^{kg} - A^{bf} C_L^{kg}(b_0^{bf})]$, where b_0^{bf}

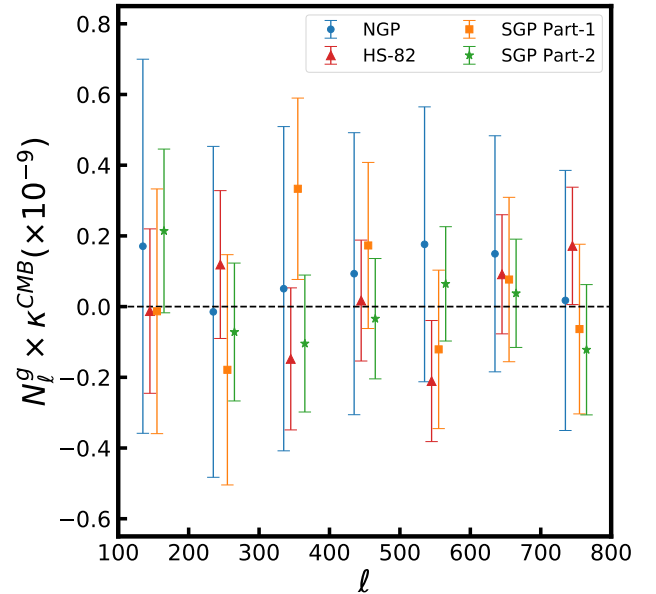


Figure 8. Mean correlation between galaxy shot noise obtained from jackknifing approach and CMB lensing convergence map. No significant signal is detected for any patch.

and A^{bf} stand for best-fit values of galaxy linear bias parameter b_0 and amplitude of cross-power spectrum A . The p -values are calculated using the standard theoretical χ^2 distribution function with $\nu = 5$ degrees of freedom. Using MV map, we obtain a value of $\chi^2/\nu \sim 0.3$ or SGP Part-1 and Part-2, ~ 1.3 for NGP and ~ 1.6 for HS-82 field. The SZ-deproj gives similar χ^2/ν values of ~ 1.4

for NGP and ~ 0.3 for SGP Part-1, while larger χ^2/ν values of ~ 0.66 for SGP Part-2 and ~ 2.1 for HS-82.

In Fig. 9, the 2-dimensional posterior distributions in the (b_0, A) plane for cross-correlation of HELP fields with MV map and corresponding marginalised distributions for each parameter are shown. For the joint analysis of the MV convergence map, we find agreement between estimated cross-correlation amplitude A and the expected value within $\sim 1\sigma$ for NGP and SGP Part-1 and within $\sim 2\sigma$ for HS-82 and SGP Part-2. For the SZ-deproj map, the amplitudes are larger and in agreement with one within $\sim 1\sigma$ for all fields, except the NGP field for which the estimated amplitude takes a value of 0.39 and the significance of the discrepancy is 2.2σ . The disparities between results for MV and SZ-deproj lensing maps can be caused by differences in the maps, in particular using CMB polarisation data for MV map and removing SZ signal from the CMB temperature map for SZ-deproj lensing map.

The estimated galaxy linear bias parameter for the joint analysis takes values the same as the ones estimated from the galaxy auto-power spectrum. It shows that the parameter is in principle entirely constrained by the latter. The parameters take values in a range from 0.70 for SGP Part-2 to 1.02 for SGP Part-1 field with less than 2% errors.

8 DISCUSSION AND CONCLUSIONS

The work presented in this paper is the first estimation of galaxy linear bias parameter b_0 and amplitude of cross-power spectrum A for the HELP catalogue. The correlation between MV CMB lensing potential and the distribution of galaxies is found to be lower than expected, but within 2σ for all patches. We now discuss possible reasons that can lead to a smaller value of the amplitude of cross-power spectrum A .

As is shown in Fig. 6 and discussed in section 7.2, we do not find any systematics in the estimation of the parameters from simulations, so we can exclude as a possible reason for observed deviation some bias introduced by algorithms used for data analysis. As a consistency check, we also applied our algorithms to the dataset used in studies presented in Bianchini et al. (2015). We reproduced the galaxy linear bias parameter and amplitude of cross-spectrum precisely within 1σ values as quoted in table 3 of Bianchini et al. (2015). This further solidifies the procedure we use to estimate parameters in this work.

8.1 CIB contamination

One possible reason for a smaller value of the amplitude can be the correlation of galaxies with residuals of Cosmic Infrared Background (CIB) emission which leaked into the lensing map through the CMB temperature maps used for the lensing estimation. As we can see in Fig. 23 from Planck Collaboration et al. (2020c), CIB-induced bias for the MV and SZ-deproj CMB lensing map auto-power spectrum is at the sub-percent level for the range of multipoles used in our analysis. Such a small CIB contribution is a result of using the SMICA CMB map for the lensing map estimation in the 2018 *Planck* data release, which significantly reduces CIB contamination. Nevertheless, it can be larger for the cross-power spectrum considered in this work. We did not estimate CIB contribution to cross-correlation leaving it for future studies, however, it is worth noticing that the redshift range of the HELP galaxies is rather low comparing to the redshifts of CIB sources, so we do not expect substantial cross-correlation between them. Because CIB-induced

bias for the SZ-deproj lensing map is roughly two times larger than for the MV lensing map, we decided to use the latter in our baseline analysis.

8.2 Magnification Bias

The second term in Eq. 7 accounts for the modification of the observed density of background sources due to weak gravitational lensing by foreground objects. We measured the value of $\alpha = 1$ for all HELP patches used in our study by fitting a straight line to $\log \mathbf{N}(> \mathbf{S})$ distribution. In this section we look at the change in parameters, b_0 and A , for $\alpha = 2$ and $\alpha = 3$. Fig. 10 presents the 2-dimensional posterior contours in the (b_0, A) plane showing change in parameters measured from SGP Part-2 for different values of α . From the joint analysis of galaxy auto-power spectrum and cross-power spectrum we get $b_0 = 0.67 \pm 0.01$ and $A = 0.67 \pm 0.18$ for $\alpha = 2$ and $b_0 = 0.64 \pm 0.01$ and $A = 0.67 \pm 0.18$ for $\alpha = 3$. Higher values of α lead to smaller values of galaxy linear bias parameter b_0 but do not affect the amplitude A . We see a similar trend also in other patches. For relatively shallow surveys such as HELP, cross-correlation with the convergence field is weak. Hence, we do not see significant changes in the cross-correlation amplitude because, for different values of α , changes in the cross-power spectrum are within the errors on data. In deeper surveys like H-ATLAS, the dependence of magnification bias on amplitude A is more prominent (see fig. 18 of Bianchini et al. 2015).

8.3 Median redshift

If the errors on redshift are large, it can lead to systematic biases in measurements and estimation of parameters from datasets. The distribution of fractional error $\frac{\sigma_z}{1+z}$ is restricted to ~ 0.15 for NGP and HS-82, and ~ 0.25 for SGP Part-1 and Part-2. Such errors can shift the peak and median of the distribution significantly from its true position. In this section, we examine the robustness of our results quoted in Tab. 3 to the median redshift of the HELP catalogue which may be misestimated due to these systematic effects. For this test, it is convenient to use some model for the redshift distributions of the HELP catalogue and check the sensitivity of the cross-correlation amplitude and galaxy bias to the parameter related to median redshift. We model the redshift distributions by a function of the form

$$\frac{dN}{dz} = a_0 z^{a_1} \exp\left[-\left(\frac{z}{a_2}\right)^{a_3}\right] \quad (31)$$

We fit parameters a_0, a_1, a_2, a_3 to the observed redshift distributions and their best fit values are given in Table 5.

The parameter a_2 is different from the median redshift z_{median} , but raising or lowering it will have a similar effect as shifting the median redshift of distribution. Thus, we use a_2 as a proxy for median redshift.

By changing the values of parameter a_2 , we recompute the theoretical power spectrum and re-estimate the parameters b_0 and A . We find that for NGP and SGP Part-1 we need around 10%, HS-82 needs $\sim 20\%$ and for SGP Part-2 we need a median redshift around 25% lower than that estimated to alleviate the tension on amplitude A . Fig. 11 shows the comparison of the 1- and 2-dimensional posteriors for SGP Part-2 field computed with 25% smaller value of the median redshift and without any change of the median.

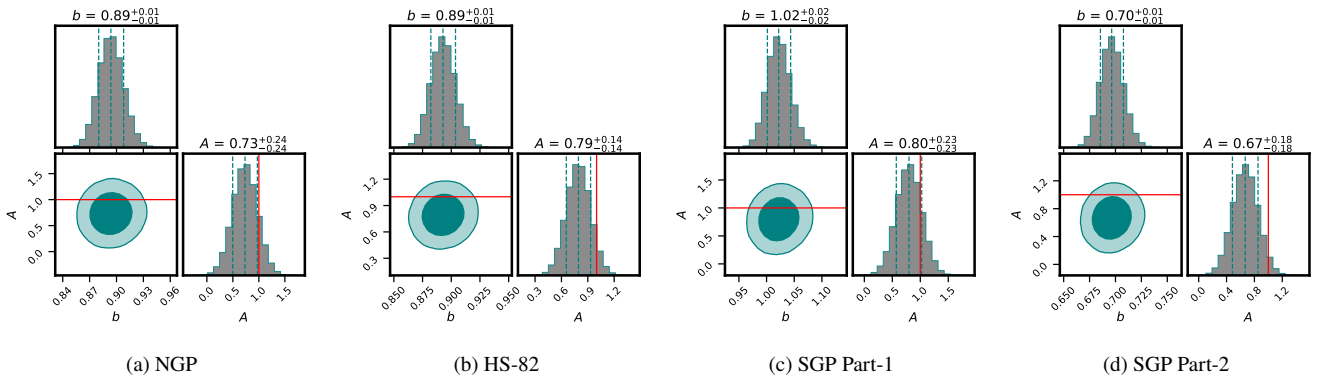
To get an idea, of whether such significant changes of the median redshift are possible for catalogue with errors of the photometric redshift of the order of $\frac{\sigma_z}{1+z} \sim 0.2$, we create mock catalogues of

Table 3. Galaxy linear bias parameter and cross-correlation amplitude for HELP patches with MV lensing potential map using both separate and joint likelihood functions.

Patch	gg	κg		$\kappa g, gg$		χ^2/ν	p -value
		b_0	A	b_0	A		
NGP	$0.89^{+0.01}_{-0.01}$	$0.97^{+0.42}_{-0.26}$	$0.61^{+0.32}_{-0.30}$	$0.89^{+0.01}_{-0.01}$	$0.73^{+0.24}_{-0.24}$	6.5/5	0.262
HS-82	$0.89^{+0.01}_{-0.01}$	$1.08^{+0.45}_{-0.27}$	$0.71^{+0.28}_{-0.25}$	$0.89^{+0.01}_{-0.01}$	$0.79^{+0.14}_{-0.14}$	8.0/5	0.155
SGP Part-1	$1.02^{+0.02}_{-0.02}$	$0.45^{+0.20}_{-0.13}$	$2.16^{+0.89}_{-0.71}$	$1.02^{+0.02}_{-0.02}$	$0.80^{+0.23}_{-0.23}$	1.4/5	0.919
SGP Part-2	$0.70^{+0.01}_{-0.01}$	$0.26^{+0.14}_{-0.10}$	$1.97^{+1.15}_{-0.72}$	$0.70^{+0.01}_{-0.01}$	$0.67^{+0.18}_{-0.18}$	1.3/5	0.938

Table 4. Galaxy linear bias parameter and cross-correlation amplitude for HELP patches with SZ-deproj lensing potential map using both separate and joint likelihood functions.

Patch	gg	κg		$\kappa g, gg$		χ^2/ν	p -value
		b_0	A	b_0	A		
NGP	$0.89^{+0.01}_{-0.01}$	$1.00^{+0.43}_{-0.27}$	$0.29^{+0.29}_{-0.28}$	$0.89^{+0.01}_{-0.01}$	$0.39^{+0.27}_{-0.27}$	6.9/5	0.229
HS-82	$0.89^{+0.01}_{-0.01}$	$1.26^{+0.51}_{-0.32}$	$0.75^{+0.29}_{-0.26}$	$0.89^{+0.01}_{-0.01}$	$1.00^{+0.14}_{-0.14}$	10.5/5	0.062
SGP Part-1	$1.02^{+0.02}_{-0.02}$	$0.50^{+0.21}_{-0.13}$	$2.34^{+0.86}_{-0.75}$	$1.02^{+0.02}_{-0.02}$	$1.04^{+0.26}_{-0.26}$	1.3/5	0.938
SGP Part-2	$0.70^{+0.01}_{-0.01}$	$0.53^{+0.23}_{-0.14}$	$1.08^{+0.45}_{-0.39}$	$0.70^{+0.01}_{-0.01}$	$0.75^{+0.21}_{-0.21}$	3.3/5	0.645

**Figure 9.** Posteriors of parameter obtained from Maximum Likelihood Estimation for all HELP patches with 68% and 95% confidence contours shown in darker and lighter shades, respectively. The three vertical lines are the median value of posterior and $\pm 1\sigma$ errors. The red line represents the value of $A = 1$ for standard Λ CDM.**Table 5.** Best fit values of a_0, a_1, a_2, a_3 for the modelling function given by Eq. 31.

Patch	a_0	a_1	a_2	a_3
NGP	5.843	1.007	0.602	3.014
HS-82	8.419	1.756	0.579	1.733
SGP Part-1	15.556	1.925	0.415	1.320
SGP Part-2	9.553	1.776	0.552	1.659

objects assuming some true redshift distribution and then randomly redistribute redshift of each object according to Gaussian probability function with standard deviation corresponding to photometric redshift errors. We generate in this way a few hundred mock catalogues and estimate the average redshift distribution for them. In the end, we compare the median redshift of the true distribution and the average one. We find that the median of the average distribution, which takes into account photometric redshift errors, is $\sim 5 - 7\%$ larger than the median of the true distribution. This difference is too

small to bring the amplitude measured for HELP patches consistent with unity.

8.4 Photometric calibration errors

Photometric calibration errors are systematics that can cause the magnitude limit of a survey to vary across the sky. This can cause changes in the number density coming from the survey across the sky. The variation in number density which does not correspond to fluctuations in physical matter density biases the galaxy overdensity power spectrum and in turn may affect the estimation of parameters. The photometric calibration error is important at large scales, but since there are different surveys combined to make the HELP catalogue, we can expect significant effects at smaller angular scales also. The calibration error can, thus, be one of the major challenges in cross-correlation studies using catalogues combined from different surveys.

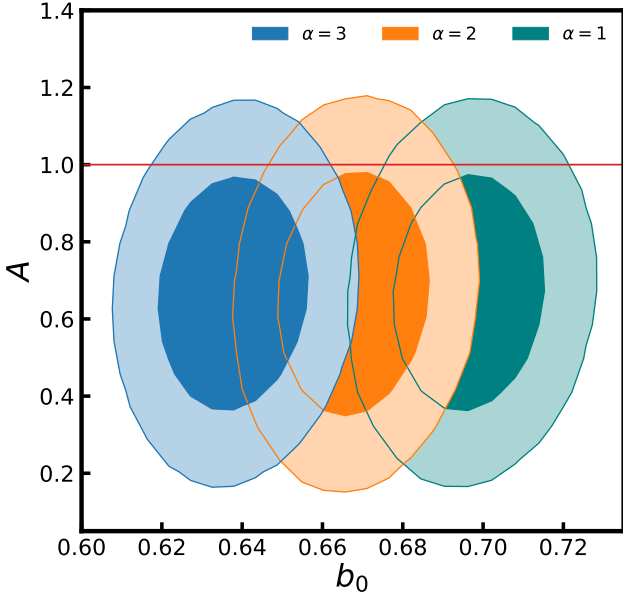


Figure 10. Effect of α on the estimated values of cross-correlation amplitude A and galaxy linear bias parameter b_0 for SGP Part-2. There is no significant effect on A .

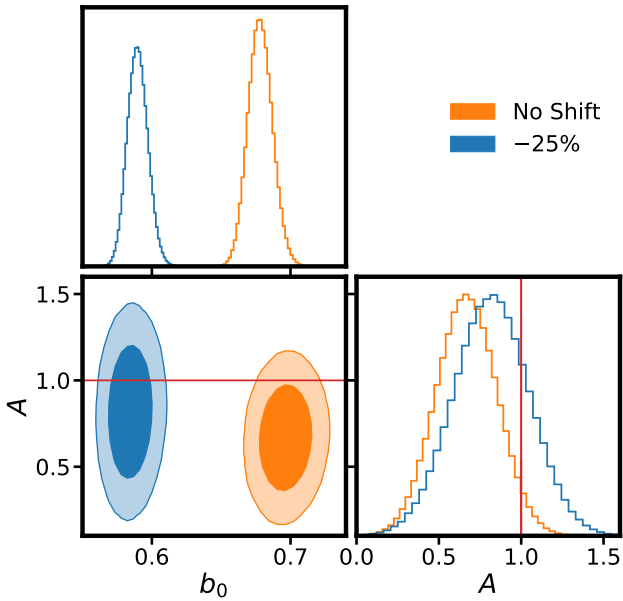


Figure 11. The parameters for SGP Part-2 computed with -25% shift in the median redshift of the distribution and without any shift. We show 68% and 95% contours with darker and lighter shaded regions, respectively. The red line represent the expected value $A = 1$.

We follow the procedure outlined in [Huterer et al. \(2013\)](#) to study the effect of calibration errors using simulations. The true galaxy number counts in a given direction of sky $N_{\text{true}}(\hat{\mathbf{n}})$ is affected by the calibration field $c(\hat{\mathbf{n}})$

$$N_{\text{obs}}(\hat{\mathbf{n}}) = [1 + c(\hat{\mathbf{n}})] N_{\text{true}}(\hat{\mathbf{n}}) \quad (32)$$

The calibration field $c(\hat{\mathbf{n}})$ can be computed using the relation

$$c(\hat{\mathbf{n}}) = \ln(10) s(z) \delta m(\hat{\mathbf{n}}) \quad (33)$$

where δm is the variation in the magnitude limit in the direction $\hat{\mathbf{n}}$ for some waveband and $s(z)$ is the faint end slope of the luminosity function given by

$$s(z) \equiv \left. \frac{d \log_{10} N(z, > m)}{dm} \right|_{m_{\text{max}}} \quad (34)$$

where m_{max} is the maximal apparent magnitude for a given waveband.

For HELP fields, we study the effects of calibration error for bands g and r as these bands are the deepest in magnitude and we also have maximum coverage for them. For a given field we simulate galaxy number count maps which include calibration field $c(\hat{\mathbf{n}})$ according to Eq. 32. Then, we estimate parameters for these simulations without correction and after correcting for the calibration errors using Eq. 32. The estimated parameters for the HS-82 field are shown in Fig. 12. As we can notice the cross-correlation amplitude remains unchanged, while the galaxy linear bias parameter is shifted up by 1 – 2 standard deviations. A similar effect is seen also for the remaining fields.

This test using simulations shows that amplitude values are robust with respect to photometric calibration errors. Nevertheless, even if they had significant impact, correction for the calibration errors would require quite a precise estimation of the calibration field. In the case of simulations, we assumed that the calibration field is known, while for real data we have only a tentative estimation of the field. For that reason, we do not apply this correction in the analysis of data.

8.5 Catastrophic photo- z error rate

In photo- z surveys, galaxies are often subject to catastrophic photo- z errors where the true value of redshift is misestimated by a significant amount. The reasons for this are not fully understood, but, like the conventional photo- z error case, the rate and outcome of catastrophic errors depend strongly on the number of photometric filters and their relation to the spectral features that carry principal information about the redshift ([Muir & Huterer 2016](#)).

We model catastrophic photo- z errors by randomly assigning estimated redshifts for a fraction x of galaxies in the HELP catalogue. For tests, we chose two different fractions of catastrophic photo- z error rates, $x = 0.01$ and 0.1 which roughly amounts to the lower and upper limits, respectively, of the fraction achieved in current surveys (see [Fang et al. 2022](#); [Jouvel et al. 2017](#); [Muir & Huterer 2016](#)). We take the range of randomized redshifts to be $z \in [0.01, 3.0]$. With randomly assigned estimated redshifts for fraction x of galaxies, we compute the redshift distribution and, hence, simulate galaxy over-density maps. We then estimate parameters b_0 and A from these simulated maps using theoretical power spectrum computed by assuming redshift distribution without catastrophic errors. Fig. 13 shows contour plots in (b_0, A) plane for simulated SGP Part-2 field corresponding to $x = 0.01$ and 0.1 . We notice that different fractions of catastrophic photo- z errors have no notable effect on the amplitude of cross-correlation A for the HELP catalogue. We see a similar trend also for other patches.

9 SUMMARY

We have presented measurement of cross-correlation between the minimum-variance and SZ-deproj CMB lensing convergence map from *Planck* 2018 data release and galaxy catalogues from the *Herschel* Extragalactic Legacy Project. For our analysis, we have

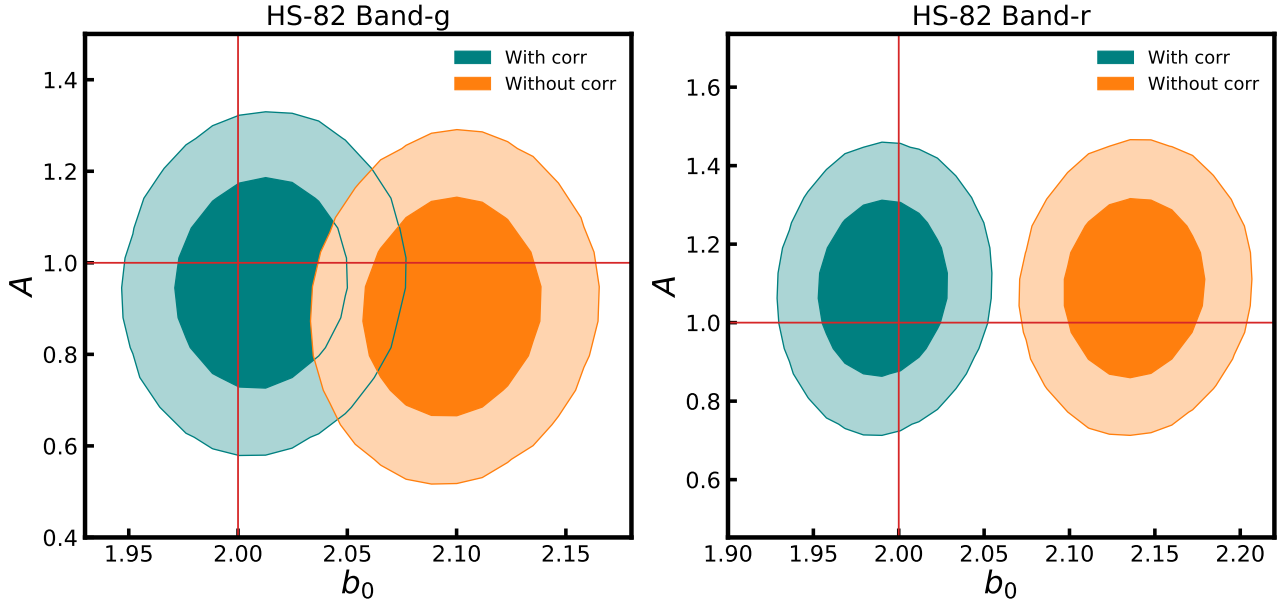


Figure 12. Comparison of estimated parameters with and without correction for the calibration error for g and r bands using simulations corresponding to HS-82 field. We show 68% and 95% contours with darker and lighter shaded regions, respectively. The red lines represent the true values of b_0 and A parameters used in simulations, i.e. $b_0 = 2$ and $A = 1$.

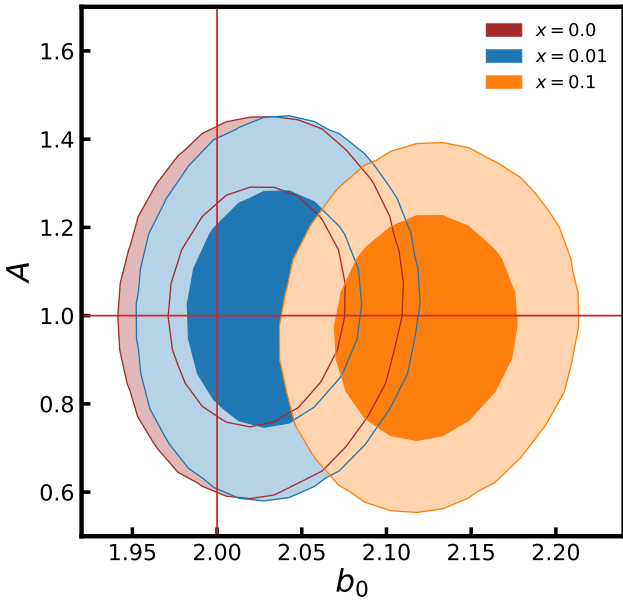


Figure 13. Effect of catastrophic errors on the inferred values of cross-correlation amplitude A and galaxy linear bias parameter b_0 for SGP Part-2. We show 68% and 95% contours with darker and lighter shaded regions, respectively, for $x = 0$ (no catastrophic errors), $x = 0.01$ and $x = 0.1$ catastrophic error rate. The red lines represent the true values of b_0 and A used in simulations ($b_0 = 2$ and $A = 1$).

selected three of the largest and most uniform fields of the catalogue namely, NGP, HS-82, and SGP divided into two parts. The areas covered by these fields are: $\sim 180 \text{ deg}^2$, $\sim 255 \text{ deg}^2$, $\sim 85 \text{ deg}^2$ and $\sim 145 \text{ deg}^2$, respectively.

We have shown that for MV lensing map the no correlation hypothesis can be ruled out with a significance of about 1.7σ for NGP, $\sim 9.2 \sigma$ for HS-82, $\sim 2.6 \sigma$ for SGP Part-1 and $\sim 2.5 \sigma$ for

SGP Part-2 field. A joint analysis of galaxy auto-power spectrum and cross-power spectrum using Maximum Likelihood approach gives the galaxy linear bias parameter for different fields ranging from $b_0 = 0.70 \pm 0.01$ for SGP Part-2 to $b_0 = 1.02 \pm 0.02$ for SGP Part-1 field. The cross-correlation amplitude varies from $A = 0.67 \pm 0.18$ for SGP Part-2 to $A = 0.80 \pm 0.23$ for SGP Part-1 field and a significance of its deviation from one is 1σ for NGP and SGP Part-1, and 2σ for HS-82 and SGP Part-2. For the SZ-deproj CMB lensing map the amplitude is higher and consistent with one for all fields, except NGP field for which its value is lower than for the MV lensing map.

Though, a significance of the deviation for the MV lensing map is not very high, especially for NGP and SGP Part-1 fields, in all cases the amplitude is biased towards lower values suggesting that there is some systematic error in the analysis. To check it we have investigated some systematic errors that can account for this deviation, such as the effect of magnification bias caused by weak gravitational lensing and catastrophic photo- z errors which were found to have no notable improvement over the detected tension of cross-correlation amplitude A . We also examined the effect of shifting the estimated median redshift of HELP galaxies and concluded that a lower effective median redshift can increase the estimated value of amplitude A , suggesting that the HELP catalogue may be shallower than expected. However, the amount of shift required to remove the observed tension on the amplitude of cross-correlation, i.e. 20-25% of the median redshift, is much larger than the potential offset related with photometric redshift errors, i.e. 5% of the median. We also found out that variations across the fields in magnitude limits of the catalogue caused by photometric calibration errors has no significant effect on the cross-correlation amplitude.

To conclude, the amplitude turned out to be robust with respect to all studied systematic errors. Only in the case of using SZ-deproj lensing map do we observe stronger cross-correlations and higher amplitude which is then consistent with one for all fields except the NGP field, which shows a weaker correlation than for MV map. These disparities can be explained by differences between MV and

SZ-deproj lensing maps, however, it also shows that we need a more robust estimation of the CMB lensing map for cross-correlation studies. We can expect that forthcoming CMB experiments and galaxy surveys will allow us to perform more robust and precise cross-correlation measurements in the future.

ACKNOWLEDGEMENTS

The authors would like to thank Raphael Shirley, Kenneth Duncan, and Katarzyna Małek for their help with different aspects of HELP data. We thank Federico Bianchini for his suggestion on the jackknifing approach to the galaxy shot noise and valuable comments. We also thank Agnieszka Pollo for valuable comments and discussions. We thank the anonymous reviewer for careful reading of the manuscript and their helpful and relevant comments which allowed us to significantly improve this paper. The work has been supported by the Polish Ministry of Science and Higher Education grant DIR/WK/2018/12 and is based on observations obtained with Planck (<http://www.esa.int/Planck>), an ESA science mission with instruments and contributions directly funded by ESA Member States, NASA, and Canada. The authors acknowledge the use of CAMB and HEALPix packages.

DATA AVAILABILITY

The HELP catalogue used in our analysis is publicly available at <http://hedam.lam.fr/HELP/dataproducts/> and the Planck 2018 data products can be obtained from <https://pla.esac.esa.int/#cosmology>. The simulated data sets in our study can be generated as described in the main text.

REFERENCES

- Aguilar Faúndez M., et al., 2019, *ApJ*, **886**, 38
 Alonso D., Bellini E., Hale C., Jarvis M. J., Schwarz D. J., 2021, *MNRAS*, **502**, 876
 Ando S., Benoit-Lévy A., Komatsu E., 2018, *MNRAS*, **473**, 4318
 Bartelmann M., Schneider P., 2001, *Phys. Rep.*, **340**, 291
 Bianchini F., Reichardt C. L., 2018, *ApJ*, **862**, 81
 Bianchini F., et al., 2015, *ApJ*, **802**, 64
 Bianchini F., et al., 2016, *ApJ*, **825**, 24
 Brammer G. B., van Dokkum P. G., Coppi P., 2008, *ApJ*, **686**, 1503
 Brown M. L., Castro P. G., Taylor A. N., 2005, *MNRAS*, **360**, 1262
 Budavári T., et al., 2003, *ApJ*, **595**, 59
 Cao Y., Gong Y., Feng C., Cooray A., Cheng G., Chen X., 2020, *ApJ*, **901**, 34
 Cawthon R., et al., 2015, in APS April Meeting Abstracts. p. Y2.003
 Darwish O., et al., 2021a, *MNRAS*, **500**, 2250
 Darwish O., et al., 2021b, *MNRAS*, **500**, 2250
 DiPompeo M. A., Myers A. D., Hickox R. C., Geach J. E., Holder G., Hainline K. N., Hall S. W., 2015, *MNRAS*, **446**, 3492
 Doux C., Penna-Lima M., Vienti S. D. P., Tréguer J., Aubourg E., Ganga K., 2018, *MNRAS*, **480**, 5386
 Efsthioiu G., 2004, *MNRAS*, **349**, 603
 Fang X., Eifler T., Schaan E., Huang H.-J., Krause E., Ferraro S., 2022, *MNRAS*, **509**, 5721
 Foreman-Mackey D., Hogg D. W., Lang D., Goodman J., 2013, *PASP*, **125**, 306
 Giusarma E., Vagnozzi S., Ho S., Ferraro S., Freese K., Kamen-Rubio R., Luk K.-B., 2018, *Phys. Rev. D*, **98**, 123526
 Górski K. M., Hivon E., Banday A. J., Wandelt B. D., Hansen F. K., Reinecke M., Bartelmann M., 2005, *ApJ*, **622**, 759

- Goto T., Szapudi I., Granett B. R., 2012, *MNRAS*, **422**, L77
 Gupta N., Reichardt C. L., 2021, *ApJ*, **923**, 96
 Han J., Ferraro S., Giusarma E., Ho S., 2019, *MNRAS*, **485**, 1720
 Hivon E., Górski K. M., Netterfield C. B., Crill B. P., Prunet S., Hansen F., 2002, *ApJ*, **567**, 2
 Hu W., 2000, *Phys. Rev. D*, **62**, 043007
 Hu W., 2001, *ApJ*, **557**, L79
 Hu W., Okamoto T., 2002, *ApJ*, **574**, 566
 Huterer D., Cunha C. E., Fang W., 2013, *MNRAS*, **432**, 2945
 Jouvel S., et al., 2017, *MNRAS*, **469**, 2771
 Kamionkowski M., Kosowsky A., Stebbins A., 1997, *Phys. Rev. D*, **55**, 7368
 Krolewski A., Ferraro S., Schlafly E. F., White M., 2020, *J. Cosmology Astropart. Phys.*, **2020**, 047
 Krolewski A., Ferraro S., White M., 2021, arXiv e-prints, p. [arXiv:2105.03421](https://arxiv.org/abs/2105.03421)
 Kuntz A., 2015, *A&A*, **584**, A53
 Lewis A., Challinor A., 2006, *Phys. Rep.*, **429**, 1
 Lewis A., Challinor A., Lasenby A., 2000, *ApJ*, **538**, 473
 Limber D. N., 1953, *ApJ*, **117**, 134
 Marques G. A., Liu J., Huffenberger K. M., Colin Hill J., 2020, *ApJ*, **904**, 182
 Millea M., et al., 2021, *ApJ*, **922**, 259
 Mo H., van den Bosch F. C., White S., 2010, Galaxy Formation and Evolution
 Muir J., Huterer D., 2016, *Phys. Rev. D*, **94**, 043503
 Namikawa T., et al., 2019, *ApJ*, **882**, 62
 Omori Y., et al., 2017, *ApJ*, **849**, 124
 Omori Y., et al., 2019a, *Phys. Rev. D*, **100**, 043501
 Omori Y., et al., 2019b, *Phys. Rev. D*, **100**, 043517
 Peacock J. A., Bilicki M., 2018, *MNRAS*, **481**, 1133
 Planck Collaboration et al., 2016, *A&A*, **594**, A24
 Planck Collaboration et al., 2020a, *A&A*, **641**, A1
 Planck Collaboration et al., 2020b, *A&A*, **641**, A6
 Planck Collaboration et al., 2020c, *A&A*, **641**, A8
 Pullen A. R., Alam S., Ho S., 2015, *MNRAS*, **449**, 4326
 Raghunathan S., Bianchini F., Reichardt C. L., 2018, *Phys. Rev. D*, **98**, 043506
 Raghunathan S., et al., 2019, *ApJ*, **872**, 170
 Schmittfull M., Seljak U., 2018, *Phys. Rev. D*, **97**, 123540
 Shirley R., et al., 2019, *MNRAS*, **490**, 634
 Shirley R., et al., 2021, *MNRAS*, **507**, 129
 Singh S., Mandelbaum R., Seljak U., Rodríguez-Torres S., Slosar A., 2020, *MNRAS*, **491**, 51
 Tristram M., Macías-Pérez J. F., Renault C., Santos D., 2005, *MNRAS*, **358**, 833
 Turner E. L., 1980, *ApJ*, **242**, L135
 Zaldarriaga M., Seljak U., 1999, *Phys. Rev. D*, **59**, 123507
 Zhang Y., et al., 2021, *MNRAS*, **501**, 1013
 de Jong J. T. A., Verdoes Kleijn G. A., Kuijken K. H., Valentijn E. A., 2013, *Experimental Astronomy*, **35**, 25

APPENDIX A: COVARIANCE MATRIX

We discuss here in detail the expression of covariance presented in Eq. 20. We start from the pseudo covariance given by

$$\begin{aligned}\widetilde{Cov}_{\ell\ell'}^{AB,CD} &= \langle (\langle \widetilde{C}_\ell^{AB} \rangle - \widetilde{C}_\ell^{AB}) (\langle \widetilde{C}_{\ell'}^{CD} \rangle - \widetilde{C}_{\ell'}^{CD}) \rangle \\ &= \langle \widetilde{C}_\ell^{AB} \widetilde{C}_{\ell'}^{CD} \rangle - \langle \widetilde{C}_\ell^{AB} \rangle \langle \widetilde{C}_{\ell'}^{CD} \rangle\end{aligned}\quad (\text{A1})$$

where \widetilde{C}_ℓ is pseudo power spectrum and A, B, C, D represent scalar fields on sky. Let $\tilde{a}_{\ell m}$ be the spherical harmonic coefficients of \widetilde{C}_ℓ .

$$\begin{aligned}\widetilde{Cov}_{\ell\ell'}^{AB,CD} &= \frac{1}{(2\ell+1)(2\ell'+1)} \sum_{mm'} \left[\langle \tilde{a}_{\ell m}^A \tilde{a}_{\ell m}^{B*} \tilde{a}_{\ell' m'}^C \tilde{a}_{\ell' m'}^{D*} \rangle - \langle \tilde{a}_{\ell m}^A \tilde{a}_{\ell m}^{B*} \rangle \langle \tilde{a}_{\ell' m'}^C \tilde{a}_{\ell' m'}^{D*} \rangle \right] \\ &= \frac{1}{(2\ell+1)(2\ell'+1)} \sum_{mm'} \left[\langle \tilde{a}_{\ell m}^A \tilde{a}_{\ell' m'}^{C*} \rangle \langle \tilde{a}_{\ell' m'}^D \tilde{a}_{\ell m}^{B*} \rangle + \langle \tilde{a}_{\ell m}^A \tilde{a}_{\ell' m'}^{D*} \rangle \langle \tilde{a}_{\ell' m'}^C \tilde{a}_{\ell m}^{B*} \rangle \right]\end{aligned}\quad (\text{A2})$$

We can express $\tilde{a}_{\ell m}$ in terms of $a_{\ell m}$, the spherical harmonic coefficients of full sky power spectrum C_ℓ , using the mode-mode coupling kernel $K_{\ell m \ell' m'}$ (Hivon et al. 2002) as:

$$\tilde{a}_{\ell m} = \sum_{\ell' m'} a_{\ell' m'} K_{\ell m \ell' m'} \quad (\text{A3})$$

with which Eq. A2 becomes

$$\begin{aligned}\widetilde{Cov}_{\ell\ell'}^{AB,CD} &= \frac{1}{(2\ell+1)(2\ell'+1)} \sum_{mm'} \sum_{\substack{\ell_1 \ell_2 \ell_3 \ell_4 \\ m_1 m_2 m_3 m_4}} \left[\langle a_{\ell_1 m_1}^A a_{\ell_2 m_2}^{C*} \rangle K_{\ell m \ell_1 m_1}^A K_{\ell' m' \ell_2 m_2}^{C*} \langle a_{\ell_3 m_3}^D a_{\ell_4 m_4}^{B*} \rangle K_{\ell' m' \ell_3 m_3}^D K_{\ell m \ell_4 m_4}^{B*} \right. \\ &\quad \left. + \langle a_{\ell_1 m_1}^A a_{\ell_3 m_3}^{D*} \rangle K_{\ell m \ell_1 m_1}^A K_{\ell' m' \ell_3 m_3}^{D*} \langle a_{\ell_2 m_2}^C a_{\ell_4 m_4}^{B*} \rangle K_{\ell' m' \ell_2 m_2}^C K_{\ell m \ell_4 m_4}^{B*} \right]\end{aligned}\quad (\text{A4})$$

Using $\langle a_{\ell m} a_{\ell' m'} \rangle = \delta_{\ell\ell'} \delta_{mm'} \langle C_\ell \rangle$, in Eq. A4, we get

$$\widetilde{Cov}_{\ell\ell'}^{AB,CD} = \frac{1}{(2\ell+1)(2\ell'+1)} \sum_{mm'} \sum_{\substack{\ell_1 \ell_4 \\ m_1 m_4}} \left[\langle C_{\ell_1}^{AC} \rangle \langle C_{\ell_4}^{DB} \rangle K_{\ell m \ell_1 m_1}^A K_{\ell' m' \ell_1 m_1}^{C*} K_{\ell' m' \ell_4 m_4}^D K_{\ell m \ell_4 m_4}^{B*} + \langle C_{\ell_1}^{AD} \rangle \langle C_{\ell_4}^{CB} \rangle K_{\ell m \ell_1 m_1}^A K_{\ell' m' \ell_1 m_1}^{D*} K_{\ell' m' \ell_4 m_4}^C K_{\ell m \ell_4 m_4}^{B*} \right] \quad (\text{A5})$$

We develop each term in Eq. A5 assuming the large sky coverage (Efstathiou 2004):

$$\sum_{\substack{\ell_1 \ell_4 \\ m_1 m_4}} \langle C_{\ell_1}^{AC} \rangle \langle C_{\ell_4}^{DB} \rangle K_{\ell m \ell_1 m_1}^A K_{\ell' m' \ell_1 m_1}^{C*} K_{\ell' m' \ell_4 m_4}^D K_{\ell m \ell_4 m_4}^{B*} = \sqrt{C_\ell^{AC} C_{\ell'}^{AC} C_\ell^{DB} C_{\ell'}^{DB}} \sum_{\substack{\ell_1 \ell_4 \\ m_1 m_4}} K_{\ell m \ell_1 m_1}^A K_{\ell' m' \ell_1 m_1}^{C*} K_{\ell' m' \ell_4 m_4}^D K_{\ell m \ell_4 m_4}^{B*} \quad (\text{A6})$$

Expanding the mode-mode coupling kernels in terms of sum over pixels and then, applying the completeness relation of spherical harmonics:

$$\begin{aligned}\sum_{\ell_1 m_1} K_{\ell m \ell_1 m_1}^X K_{\ell' m' \ell_1 m_1}^{Y*} &= \sum_{\ell_1 m_1} \sum_{pq} w_p^X w_q^{Y*} \Omega_p \Omega_q Y_{\ell m}(\theta_p) Y_{\ell_1 m_1}^*(\theta_p) Y_{\ell_1 m_1}(\theta_q) Y_{\ell' m'}^*(\theta_q) \\ &= \sum_{pq} w_p^X w_q^{Y*} \Omega_p \Omega_q Y_{\ell m}(\theta_p) Y_{\ell' m'}^*(\theta_q) \frac{\delta(\theta_p - \theta_q)}{\Omega_q} \\ &= \sum_p w_p^{XY} \Omega_p Y_{\ell m}(\theta_p) Y_{\ell' m'}^*(\theta_p) \\ &= K_{\ell m \ell' m'}^{XY}\end{aligned}\quad (\text{A7})$$

where w_p is an arbitrary weight function, Ω_p is area of each pixel and we have defined $w_p^{XY} = w_p^X w_p^{Y*}$ as another arbitrary weight function. With Eq. A6 and Eq. A7, Eq. A5 simplifies as:

$$\widetilde{Cov}_{\ell\ell'}^{AB,CD} = \frac{1}{(2\ell+1)(2\ell'+1)} \sum_{mm'} \left[\sqrt{C_\ell^{AC} C_{\ell'}^{AC} C_\ell^{DB} C_{\ell'}^{DB}} K_{\ell m \ell' m'}^{AC} K_{\ell m \ell' m'}^{BD*} + \sqrt{C_\ell^{AD} C_{\ell'}^{AD} C_\ell^{CB} C_{\ell'}^{CB}} K_{\ell m \ell' m'}^{AD} K_{\ell m \ell' m'}^{BC*} \right] \quad (\text{A8})$$

The product of coupling kernels can be expanded in terms of Wigner-3j symbols as:

$$\begin{aligned} \sum_{mm'} K_{\ell m \ell' m'}^{AC} K_{\ell m \ell' m'}^{BD*} &= \sum_{mm'} \sum_{\substack{\ell_1 \ell_2 \\ m_1 m_2}} w_{\ell_1 m_1}^{AC} w_{\ell_2 m_2}^{BD*} \frac{(2\ell+1)(2\ell'+1)}{4\pi} \sqrt{(2\ell_1+1)(2\ell_2+1)} \\ &\times \begin{pmatrix} \ell & \ell' & \ell_1 \\ 0 & 0 & 0 \end{pmatrix} \begin{pmatrix} \ell & \ell' & \ell_2 \\ 0 & 0 & 0 \end{pmatrix} \begin{pmatrix} \ell & \ell' & \ell_1 \\ m & -m' & m_1 \end{pmatrix} \begin{pmatrix} \ell & \ell' & \ell_2 \\ m & -m' & m_2 \end{pmatrix} \end{aligned} \quad (\text{A9})$$

Using the orthogonality relations of Wigner-3j symbols, Eq. A9 simplifies as

$$\sum_{mm'} K_{\ell m \ell' m'}^{AC} K_{\ell m \ell' m'}^{BD*} = (2\ell+1) M_{\ell \ell'}^{AC, BD} \quad (\text{A10})$$

where $M_{\ell \ell'}^{AB, CD}$ is given by (Hivon et al. 2002)

$$M_{\ell \ell'}^{AB, CD} = \frac{2\ell'+1}{4\pi} \sum_{\ell_1} (2\ell_1+1) \left[\frac{1}{2\ell_1+1} \sum_{m_1} w_{\ell_1 m_1}^{AC} w_{\ell_2 m_2}^{BD*} \right] \begin{pmatrix} \ell & \ell' & \ell_1 \\ 0 & 0 & 0 \end{pmatrix}^2 \quad (\text{A11})$$

This transforms the expression for pseudo covariance matrix Eq. A8 as

$$\widetilde{Cov}_{\ell \ell'}^{AB, CD} = \frac{1}{(2\ell'+1)} \left[M_{\ell \ell'}^{AC, BD} \sqrt{C_{\ell}^{AC} C_{\ell'}^{AC} C_{\ell}^{DB} C_{\ell'}^{DB}} + M_{\ell \ell'}^{AD, BC} \sqrt{C_{\ell}^{AD} C_{\ell'}^{AD} C_{\ell}^{CB} C_{\ell'}^{CB}} \right] \quad (\text{A12})$$

The binned covariance matrix for full-sky is given by (Brown et al. 2005):

$$Cov_{LL'}^{AB, CD} = (M_{LL_1}^{AB^{-1}} P_{L_1, \ell}) \left[\frac{M_{\ell \ell'}^{AC, BD} \sqrt{C_{\ell}^{AC} C_{\ell'}^{AC} C_{\ell}^{DB} C_{\ell'}^{DB}} + M_{\ell \ell'}^{AD, BC} \sqrt{C_{\ell}^{AD} C_{\ell'}^{AD} C_{\ell}^{CB} C_{\ell'}^{CB}}}{(2\ell'+1)} \right] (M_{L'L_2}^{CD^{-1}} P_{L_2, \ell'})^T \quad (\text{A13})$$

Eq. A13 is similar to that obtained by Tristram et al. (2005). This expression takes into account different fractions of sky covered by the fields A, B, C, D .

This paper has been typeset from a $\text{\TeX}/\text{\LaTeX}$ file prepared by the author.